



Evaluation of small-scale yielding boundary using digital image correlation results

Jose M. Vasco-Olmo¹  | Francisco A. Díaz¹  | Diogo M. Neto² |
Edmundo R. Sérgio² | Fernando V. Antunes² | M. Neil James^{3,4}

¹Department of Mechanical and Mining Engineering, University of Jaén, Jaén, Spain

²Univ Coimbra, Centre for Mechanical Engineering, Materials and Processes (CEMMPRE), Department of Mechanical Engineering, University of Coimbra, Coimbra, Portugal

³School of Engineering, University of Plymouth, Plymouth, UK

⁴eNtisa, Nelson Mandela University, Port Elizabeth, South Africa

Correspondence

Fernando V. Antunes, Univ Coimbra, Centre for Mechanical Engineering, Materials and Processes (CEMMPRE), Department of Mechanical Engineering, University of Coimbra, Coimbra, Portugal.
Email: fernando.ventura@dem.uc.pt

Funding information

Junta de Andalucía, Grant/Award Number: 1380786; Foundation for Science and Technology, Grant/Award Numbers: UIDB/00285/2020, PTDC/EME-EME/31657/2017

Abstract

In this work, the boundaries of small-scale yielding (SSY) and large-scale yielding (LSY) have been experimentally evaluated from the analysis of crack tip opening displacement (CTOD) measured by digital image correlation (DIC). According to a previous numerical work, the ratio between the elastic CTOD range and the total CTOD range ($\Delta\delta_e/\Delta\delta_t$) defines the boundaries of SSY conditions and LSY. Three materials have been studied, commercially pure titanium and 2024-T3 and 7050-T6 aluminum alloys, tested at different stress ratio values. SSY conditions are shown to dominate when $\Delta\delta_e/\Delta\delta_t \geq 79\%$ and $\geq 78\%$ for titanium and the two aluminum alloys, respectively. In addition, LSY can be established when $\Delta\delta_e/\Delta\delta_t \leq 66.3\%$ and $\leq 67.2\%$ for titanium and for 2024-T3 and 7050-T6 aluminum alloys, respectively. Transition or LSY conditions are more probable in fatigue tests conducted at low R ratio and for crack lengths above 40% with respect to the width of the specimen.

KEYWORDS

crack tip opening displacement, digital image correlation (DIC), fatigue crack propagation, large-scale yielding (LSY), linear elastic fracture mechanics, small-scale yielding (SSY), stress intensity factor

1 | INTRODUCTION

The stress intensity factor, K , quantifies the strength of stress and strain singularity at a crack tip, in linear elastic materials. Its range, ΔK , has been widely used to study fatigue crack growth since Paris–Erdogan law.¹ The inability to explain the R effect and the odd results observed for short cracks or variable amplitude loading forced the appearance of crack closure concept.² This approach assumes that the crack driving force is the effective stress intensity factor range: $\Delta K_{eff} = K_{max} - K_{open}$, being K_{max} and K_{open} the maximum and the crack opening stress intensity factors,

respectively. A significant number of models was subsequently proposed including other parameters, namely, fatigue threshold, fracture toughness,^{3,4} Young's modulus, yield stress,^{5,6} and hardening exponent.⁷ After 1993, different authors proposed alternative concepts based on ΔK and K_{max} , instead of ΔK_{eff} , namely, Vasudevan et al.⁸ (Unified approach), Kujawski,⁹ and Noroozi et al.¹⁰ (UniGrow approach). Christopher et al.¹¹ proposed a novel mathematical model of the stresses around the tip of a fatigue crack (CJP model), which considers the effects of wake contact and compatibility-induced stresses at the elastic–plastic boundary on the surrounding elastic field. The effective stress field is characterized by: an

opening mode stress intensity factor K_F that drives crack growth, a retarding stress intensity factor, K_R and the T stress.

All previous models retain the concept of dominance of a stress intensity parameter in the near crack tip region and assume that linear elastic fracture mechanics (LEFM) applies, that is, that the concept of similitude will hold true. The dominance of K -based approaches in fatigue studies in the last six decades may be explained by the advantages of their use, namely: (i) There are international standards (ASTM E647¹²; ISO 12108¹³), which present K solutions for the compact tension (CT) and MT specimens usually used in the experimental tests. (ii) The researchers devoted to experimental analysis can develop an independent work, without the need of a parallel numerical analysis. The basic experimental equipment includes a testing machine with adequate grips, and an optical microscope to measure the crack length. (iii) The major part of fatigue crack growth (FCG) studies have been developed using da/dN - ΔK curves; therefore, there are many results in literature for comparison. (iv) K solutions are available in literature for different cracked geometries.^{14–16} Additionally, the numerical determination of K is relatively simple using commercial FEM software. (v) The K -based models include the effects of all crack tip damage mechanisms, like oxidation, cyclic plastic deformation, or coalescence of microvoids. The complexity of the FCG phenomenon is therefore greatly simplified, although this entails a loss of knowledge about what goes on at the crack tip.

However, plastic deformation is usually observed at the crack tip in metallic materials, which affects crack tip fields. If this plastic deformation is very high, the validity of ΔK parameter is questionable. A boundary for small-scale yielding (SSY) regime must be defined to apply ΔK with confidence. The ASTM E647-15 standard¹² states that for results of K calculation to be valid, the dimensions of CT and MT specimens should meet the following criteria, respectively:

$$(W - a) \geq \frac{4}{\pi} \left(\frac{K_{max}}{Y_0} \right)^2 \quad (1)$$

$$(W - 2a) \geq 1.25 \left(\frac{F_{max}}{tY_0} \right)^2 \quad (2)$$

where K_{max} is the maximum stress intensity factor, F_{max} is the maximum force, W is the width of specimen, t is the thickness of specimen, a is the crack length and Y_0 is the yield stress of the material. This criterion indicates that the non-cracked ligament of the specimen must be relatively large, in order to give space for the

K dominated region. Alternatively, the definition of SSY regime have been defined comparing the plastic zone size with crack length ($r_p < a$).¹⁷ However, most of the times the validity of SSY regime is not checked.

The experimental and numerical tools have evolved in such a way that it is now possible to look directly to the crack tip, where fatigue crack growth (FCG) really happens. This permits a jump to a new level of understanding of FCG. In previous work of the authors,¹⁸ the elastic and total crack tip opening displacement (CTOD) ranges, $\Delta\delta_e$ and $\Delta\delta_t$, respectively, predicted numerically at a small distance behind crack tip (8 μm), were used to define a new parameter:

$$\% \Delta\delta_e = \frac{\Delta\delta_e}{\Delta\delta_t} \times 100 \quad (3)$$

Figure 1 is a schematic representation of a CTOD curve, showing the elastic and plastic CTOD ranges.¹⁹ The total CTOD, $\Delta\delta_t$, is the sum of elastic and plastic components.

The lower boundary of SSY regime was proposed to be $\% \Delta\delta_e$ equal to 75%, and the upper boundary of LSY was proposed to exist for $\% \Delta\delta_e$ equal to 60%.¹⁸ In fact, the CTOD is able to feel crack tip phenomena; therefore, is ideal to understand the extension of crack tip plastic deformation. This concept was applied to notched samples and it was found that a significant number of cases studied fall outside the SSY regime.²⁰ Escalero et al.²¹ followed a similar approach, using the J integral. The boundary of SSY was defined by the separation of two J -integral curves obtained for elastic and elastic-plastic

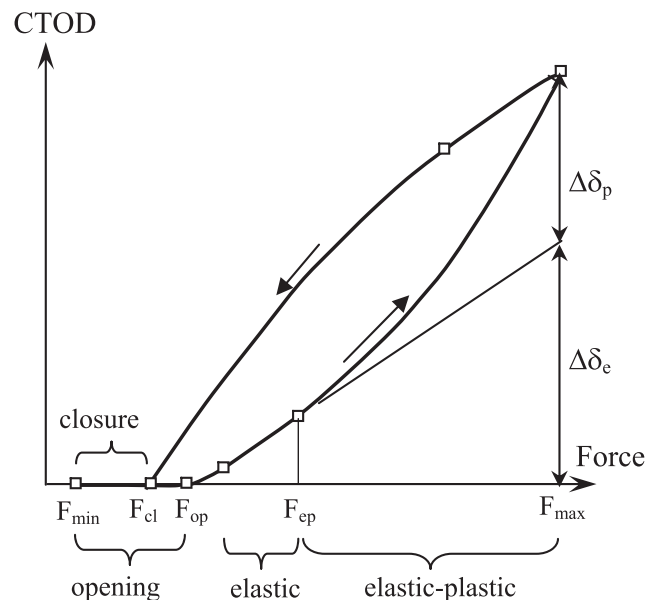


FIGURE 1 Schematic representation of crack tip opening displacement (CTOD) versus load curve

material models. An arbitrary criterion of a difference of 2% was considered.

Digital image correlation (DIC) is now being widely used in experimental studies of FCG. The analysis of SSY boundary using DIC is very interesting, avoiding the need of complementary numerical studies. However, the approach proposed by Marques et al.,¹⁸ based on COTD, was defined for a measurement point at a distance of 8 μm behind crack tip. The digital extensometers defined in DIC studies can only be placed at larger distances behind crack tip; therefore, the limits for the SSY and LSY boundaries must be redefined. Therefore, a numerical approach will be followed here to define an evolution of the criterion proposed by Marques et al.,¹⁸ in order to include the effect of the position of the measuring point relatively to the crack tip. The criterion will be subsequently applied to DIC results obtained in titanium and aluminum alloys.

2 | NUMERICAL ANALYSIS

2.1 | Numerical model

Standard compact C(T) specimens were used in this work, as illustrated in Figure 2A. The specimen is symmetrical in both the vertical and horizontal planes, and therefore, only 1/4 of the specimen has to be simulated using appropriate boundary conditions (Figure 2B). A

small specimen thickness was used ($t = 0.1 \text{ mm}$) to give a plane stress state. The application of the load is made vertically at the hole, as indicated, avoiding rigid body movement along horizontal direction.

Four materials were considered: the Ti6Al4V titanium alloy, and the 2024-T351, 2050-T8 and 7050-T6 aluminum alloys. Elastic–plastic models were used for these materials. In these simulations the elastic behavior followed a generalized Hooke's law and plastic behavior was governed by the Huber–Mises yield criterion coupled with isotropic and kinematic hardening, under an associated flow rule. The kinematic behavior is given by the Armstrong–Frederick hardening law²²:

$$\dot{\mathbf{X}} = C_X \left[X_{\text{Sat}} \frac{\sigma' - \mathbf{X}}{\bar{\sigma}} - \mathbf{X} \right] \dot{\bar{\epsilon}}^p \quad (4)$$

where C_X and X_{Sat} are the material parameters of Armstrong–Frederick law, σ' is the Cauchy stress tensor, \mathbf{X} is the back stress tensor, $\bar{\sigma}$ is the equivalent stress and $\dot{\bar{\epsilon}}^p$ is the equivalent plastic strain rate.

Table 1 gives the isotropic behavior for the various materials in terms of the Voce hardening law,²⁵ as follows:

$$Y = Y_0 + (Y_{\text{Sat}} - Y_0)[1 - \exp(-C_Y \bar{\epsilon}^p)] \quad (5)$$

where Y_0 is the yield stress, Y_{Sat} , and C_Y are material parameters in the Voce law and $\bar{\epsilon}^p$ is the equivalent

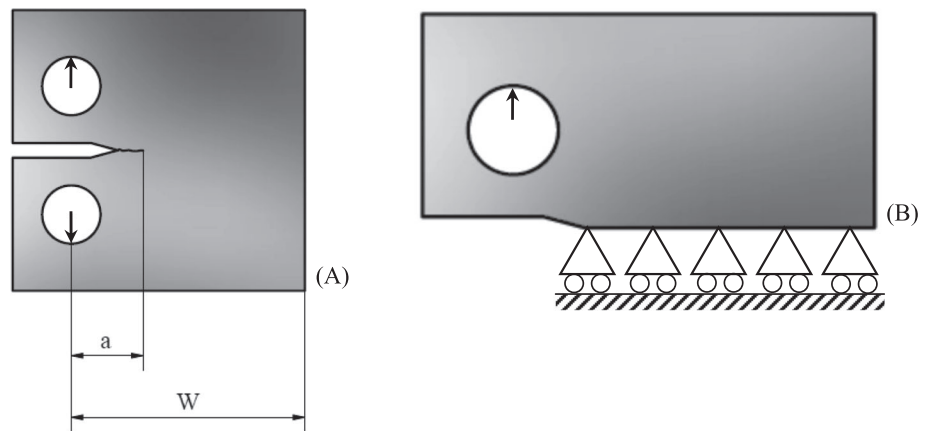


FIGURE 2 Compact tension (CT) specimen (A) main dimensions. (B) Boundary conditions

TABLE 1 Material properties with isotropic hardening fitted with Voce law

Material	Hooke's law		Isotropic hardening (Voce)		Kinematic hardening (Armstrong–Frederick)		
	E (GPa)	ν (—)	Y_0 (MPa)	Y_{Sat} (MPa)	C_Y (—)	C_X (—)	X_{Sat} (MPa)
2050-T8 ²³	70.40	0.30	383.9	383.85	0	95.38	265.41
7050-T6 ²⁴	69.724	0.30	420.5	420.5	3.806	228.91	198.35

plastic strain. Table 2 gives the equivalent isotropic behavior of the materials in terms of the Swift hardening law,²⁸ as follows:

$$Y = C \left[\left(\frac{Y_0}{C} \right)^{\frac{1}{n}} + \bar{\epsilon}^p \right]^n \quad (6)$$

where C and n are material parameters in the Swift law. The values of the elastic–plastic properties found in Tables 1 and 2 were obtained by fitting experimentally obtained cyclic stress–strain loops from smooth cylindrical specimens.

The finite-element mesh was refined near the crack tip and enlarged for more remote positions. Square elements with dimensions of $8 \times 8 \mu\text{m}^2$ were used in the crack propagation region. This element size was chosen as a compromise between increased computation time with a smaller mesh size and the first node being relatively too far from the crack tip with a larger mesh size. Only one layer of elements was considered through the thickness. Crack propagation was simulated by successive debonding of nodes at the minimum load, which

occurred when the cumulative plastic strain at the crack tip reaches a critical value. Each crack increment corresponded to one finite element, and the crack propagates uniformly through the thickness by releasing both current crack front nodes. The numerical simulations were performed with the three-dimensional elastic–plastic finite-element program DD3IMP, originally developed to simulate deep drawing. Further details of this numerical procedure may be found in the literature.²⁹

2.2 | Numerical results

Figure 3A presents typical CTOD plots obtained at distances of 8 and 96 μm from the crack tip, measured along crack flank. A huge effect of measurement point is evident. At the first node behind crack tip ($L_x = 8 \mu\text{m}$), after crack opening there is a well-defined loop, which is a consequence of crack tip plastic deformation. At a larger distance from crack tip, the crack opens at lower load values and the maximum CTOD is significantly higher. The loop is barely noticeable, which indicates a lower level of plastic deformation. Because the plastic

TABLE 2 Material properties with isotropic hardening fitted with Swift law

Material	Hooke's law		Isotropic hardening (Swift)			Kinematic hardening (Armstrong–Frederick)	
	E (GPa)	ν (—)	Y_0 (MPa)	C (MPa)	n (—)	C_x (—)	X_{Sat} (MPa)
2024-T351 ²⁶	72.261	0.29	288.96	389	0.056	138.8	111.84
Ti6Al4V HIP ²⁷	115	0.33	823.50	707.07	−0.0288	104.26	402.01

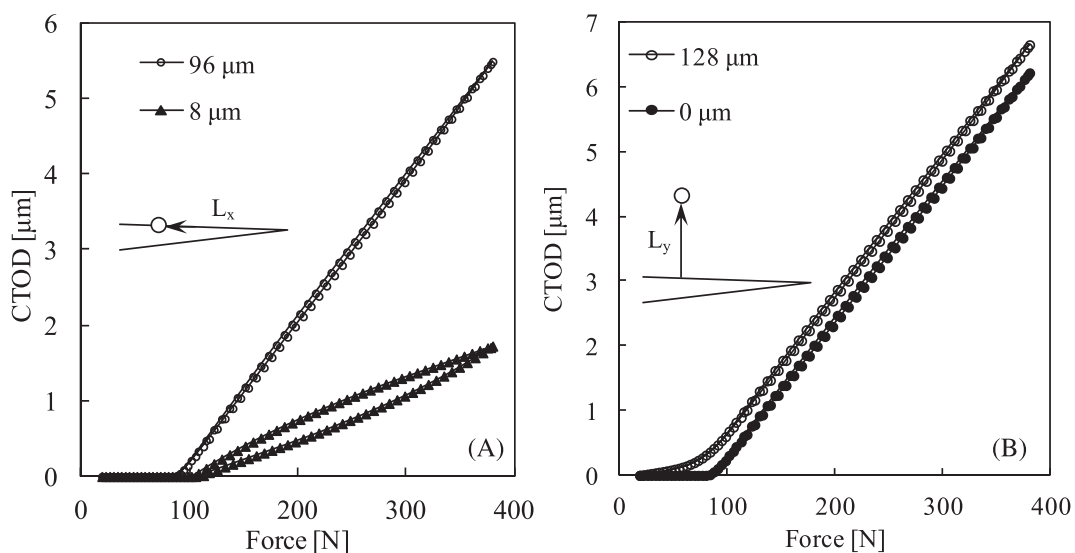


FIGURE 3 Crack tip opening displacement (CTOD) versus load curves. (A) Effect of distance to crack tip along crack flanks, L_x ($L_y = 0$). (B) Effect of distance to crack tip perpendicularly to crack flanks, L_y ($L_x = 120 \mu\text{m}$). (AA7050-T6; $W = 50 \text{ mm}$, plane stress; $\Delta K = 15.5 \text{ MPa}\cdot\text{m}^{0.5}$; $da/dN = 0.4 \mu\text{m}/\text{cycle}$)

deformation at the crack tip is the same, these results indicate that moving away from the crack tip there is a decrease of sensitivity relatively to crack tip phenomena. On the other hand, there is an increase of elastic deformation.

Figure 3B illustrates the effect of the position of measurement point relatively to crack flank. The increase of L_y does not affect significantly the aspect of the CTOD curves. The crack opens first and the maximum CTOD is slightly higher, but the loop is not visible at both measurement points. Therefore, the distance L_y , indicated schematically in Figure 3B, is not expected to affect the sensitivity to crack tip plastic deformation.

Figure 4A presents the variations of elastic and plastic CTOD ranges, $\Delta\delta_e$ and $\Delta\delta_p$, respectively, with the distance of measurement point behind crack tip, L_x . The increase of L_x produces an increase of elastic deformation, which is linked to crack opening profile. On the other hand, there is a decrease of plastic CTOD range, which means that the separation of the measuring point relatively to the crack tip results in a loss of sensitivity to what goes on there. The variation is very steep for low values of L_x , less than 50 μm , being smoother for longer distances. The same trend is observed for the elastic CTOD, but less pronounced. Note also that the plastic CTOD is significantly lower than the elastic CTOD even at the first node behind crack tip, but this depends on the material and load level. The ratio between elastic and total CTOD is presented in Figure 4B. There is a sudden increase of $\% \Delta\delta_e = \Delta\delta_e / \Delta\delta_t$, up to $L_x = 50 \mu\text{m}$, from which a smooth variation is observed. The CT specimen studied has SSY conditions because $\% \Delta\delta_e$ is higher than 75% at the first node behind crack tip ($L_x = 8 \mu\text{m}$).

Figure 5A shows the effect of crack length on $\% \Delta\delta_e$ for the Ti6Al4V alloy. CTOD values measured at the first node behind crack tip are superimposed, showing that the increase of crack length from 12.5- to 16-mm increase the total CTOD, which could be expected because the CT specimen becomes less stiff. The plastic CTOD also increases with crack length, due to the increase of the strength of stress singularity at the crack tip. The variation of plastic CTOD is dominant over the increase of elastic CTOD; therefore, there is a decrease of $\Delta\delta_e / \Delta\delta_t$ with crack length, as observed in Figure 5A. Figure 5B shows the effect of stress ratio, R , on the elastic and plastic CTOD. The increase of R from 0.05 to 0.4 increases both $\Delta\delta_e$ and $\Delta\delta_t$, which is explained by crack closure phenomenon. CTOD values measured at the first node behind crack tip are superimposed, showing the elimination of crack closure phenomenon with the increase of stress ratio. However, the parameter $\Delta\delta_e / \Delta\delta_t$ does not change with R for this material.

3 | EXPERIMENTAL WORK

The experimental work used 1-mm thick CT specimens (dimensions shown in Figure 6) manufactured from sheets of commercially pure titanium and 2024-T3 and 7050-T6 aluminum alloys. Young's modulus is 105, 72.3, and 71.7 GPa, for the titanium, AA2024-T3, and AA7050-T6, respectively, while the yield stress is 390, 348, and 420 MPa, respectively. Two titanium specimens were tested in constant amplitude fatigue loading with a maximum load of 750 N at stress ratio values of 0.1 and 0.6. In the case of the aluminum specimens, three

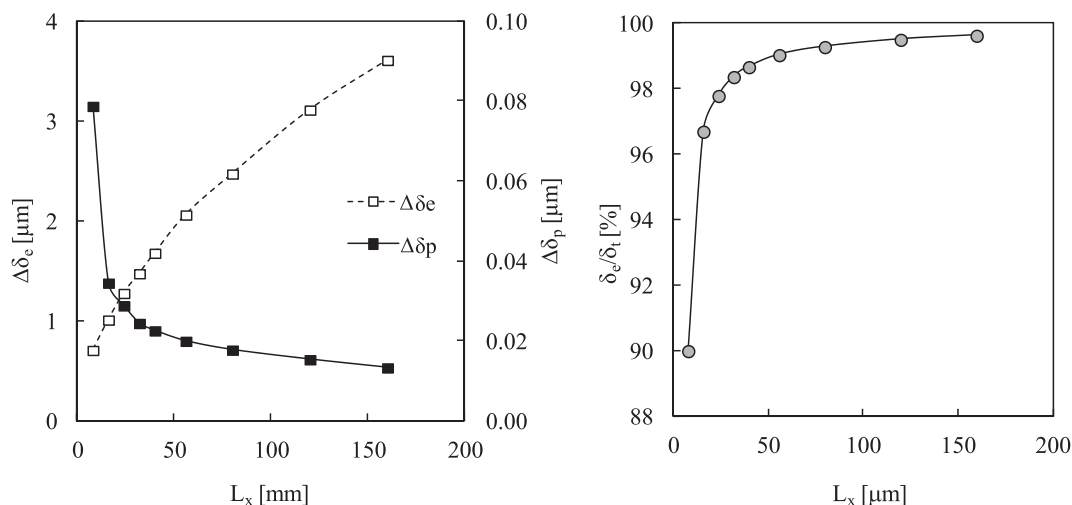


FIGURE 4 (A) Effect of distance to crack tip on elastic and plastic crack tip opening displacement (CTOD) ranges. (B) Effect of distance to crack tip on the ratio between $\Delta\delta_e$ and $\Delta\delta_t$. (AA2050-T8; CT; $W = 36 \text{ mm}$; $a = 8.272 \text{ mm}$; plane stress; $\Delta K = 11.3 \text{ MPa}\cdot\text{m}^{0.5}$; $R = 0.05$; $dy = 0$)

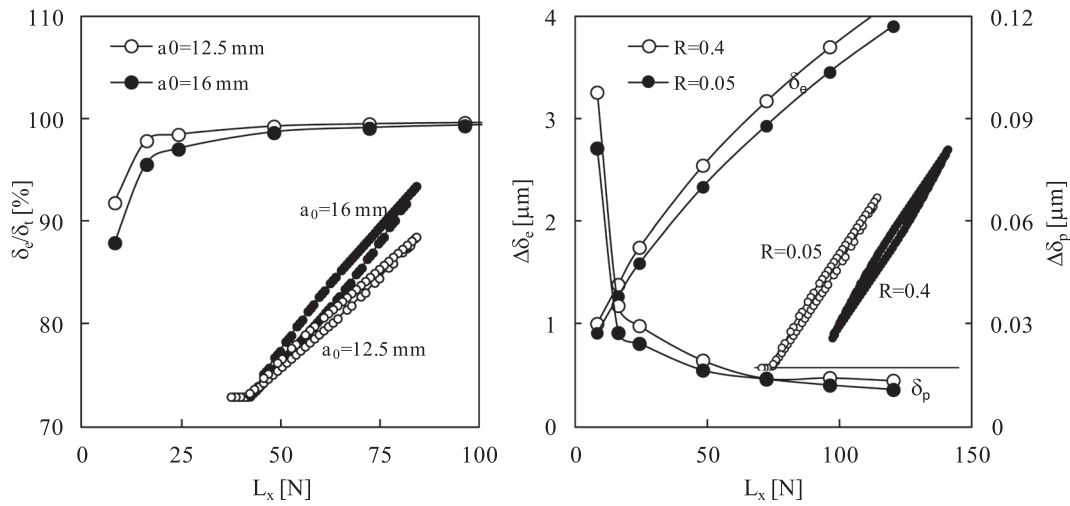


FIGURE 5 (A) Effect of crack length on $\Delta\delta_e/\Delta\delta_t$ (Ti6Al4V; $R = 0.05$; $F_{max} = 44.05$ N; $F_{min} = 2.2$ N). (B) Effect of stress ratio on elastic and plastic crack tip opening displacement (CTOD) (Ti6Al4V; $a_0 = 12.5$ mm; $\Delta K = 15.0$ MPa.m^{0.5})

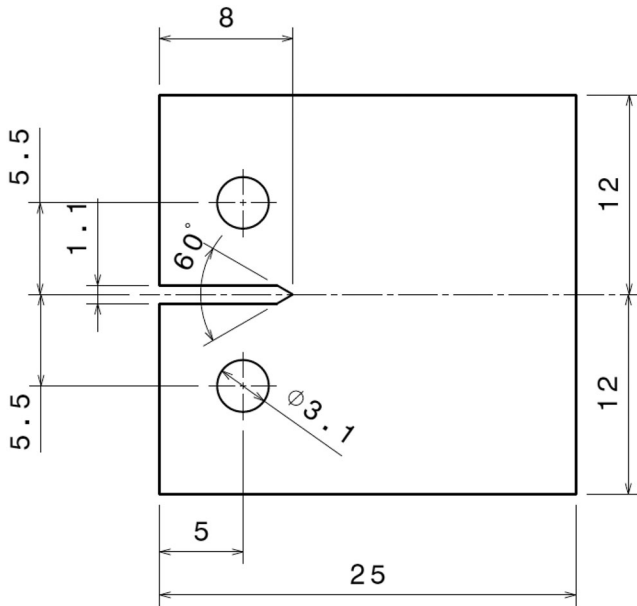


FIGURE 6 Dimensions (mm) of the compact tension (CT) specimens (ASTM E647)

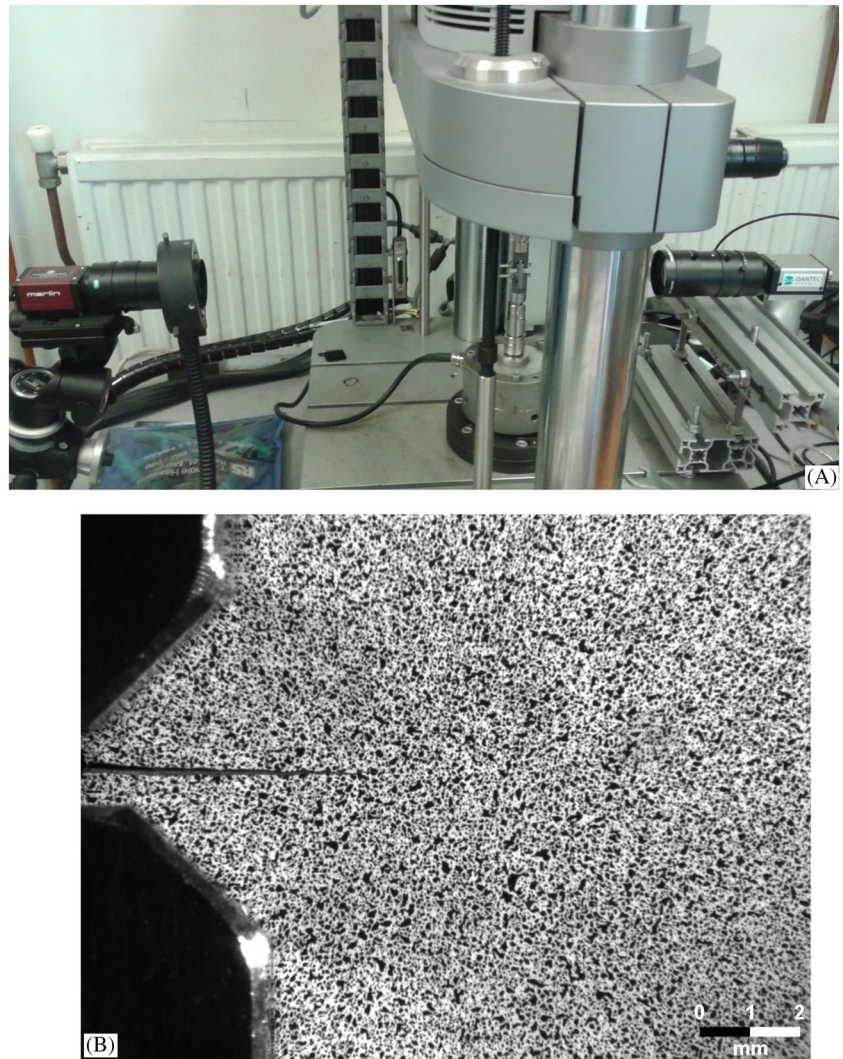
fatigue tests for each alloy were conducted at R -ratio values of 0.1, 0.3, and 0.5 applying a maximum load of 600 N.

Fatigue tests for the titanium specimens were conducted on an electrodynamic machine (Instron Electropuls E3000) with a loading capacity of 3 kN, while a 25-kN servohydraulic machine (MTS 370.02) was used for the aluminum specimens. All fatigue tests were performed at a loading frequency of 10 Hz. The experimental setup used to conduct the fatigue tests and perform data acquisition for the titanium specimens is shown in Figure 7A. A very similar setup was arranged for fatigue

tests conducted with the aluminum specimens. A random black speckle (shown in Figure 7B) was sprayed with an airbrush over a white background on one of the surface of each specimen to implement DIC. A charge-coupled device (CCD) camera, fitted with a macro-zoom lens to increase the spatial resolution around the region surrounding the crack tip, was placed perpendicularly to each side of the specimen. The camera placed in the speckled surface was used for the DIC measurements, while the other camera was used to track the crack tip for the different crack lengths analyzed. The camera system was arranged to visualize the crack propagation at the center of the image (as seen in Figure 7B), with a resolution of 13.7 $\mu\text{m}/\text{pixel}$ in the case of the titanium specimens and 8.8 $\mu\text{m}/\text{pixel}$ for the aluminum specimens, corresponding with a field of view of 17.3×13 mm and 14.1×10.6 mm, respectively. An optic fiber light ring was placed around the zoom lens (also shown in Figure 7B) to illuminate the speckled surface of the specimen and to assist better observation of the speckle pattern and improved image processing.

In CTOD measurement, a particularly important aspect and in the consistency of the results is ensuring accurate location of the crack tip. According to this, an experimental methodology for its location was published by the present authors in a previous work.³⁰ Vertical displacement fields obtained by DIC were used to measure the CTOD selecting a pair of points behind the crack tip to measure the relative displacement between the crack flanks. Figure 8 shows an example of the displacement fields obtained for the AA7050-T6 specimen tested at $R = 0.1$ corresponding to a load of 600 N and a 9.13-mm crack. The developed methodology consisted of found the x and y coordinates of the crack tip from the analysis of

FIGURE 7 (A) Experimental setup used to conduct the fatigue tests and for data acquisition. (B) Speckle pattern sprayed onto one of the specimen surfaces to implement digital image correlation (DIC) [Colour figure can be viewed at wileyonlinelibrary.com]



different vertical displacement profiles plotted in the perpendicular and parallel directions of the crack plane.

Besides the accurate crack tip location, other critical aspect in the interpretation of CTOD data is the location of the pair of points selected behind the crack tip to measure the CTOD. For this reason, a sensitivity analysis was performed by the present authors in a previous work³⁰ to explore how the x and y positions can affect the CTOD value. As shown in Figure 9, two distances behind the crack tip were used to define the CTOD measurement position, one parallel with the crack direction (defined as L_x) and other one perpendicular to the crack plane (defined as L_y). In the sensitivity analysis, it was evaluated the variation of the CTOD values obtained at maximum load corresponding to a range for one of the measurement distances, while keeping the other distance fixed. This analysis indicated that the CTOD could be precisely measured using data obtained from two measurement points located behind the crack tip at distances of $L_x = 123.2 \mu\text{m}$ and $L_y = 132 \mu\text{m}$ for the aluminum

specimens and $L_x = 68.4 \mu\text{m}$ and $L_y = 136.8 \mu\text{m}$ for the titanium specimens.

4 | EXPERIMENTAL RESULTS

Once the values of L_x and L_y measurement distances have been established, the CTOD can be resolved into its elastic and plastic components from an analysis of a full loading cycle. A typical plot of CTOD data at increments of 20 N throughout a full loading cycle for a crack length of 9.13 mm in the case of the 7050-T6 aluminum specimen tested at $R = 0.1$ is shown in Figure 10. The analysis of the different behaviors observed (indicated with upper case letters) during the load cycle allows the range of elastic and plastic CTOD to be obtained. The loading part of the cycle between Points A and B (60 to 140 N) is associated with crack opening. Once the crack is open, there is a linear regime between Points B and C (140 and 320 N), which is attributed to the elastic response.

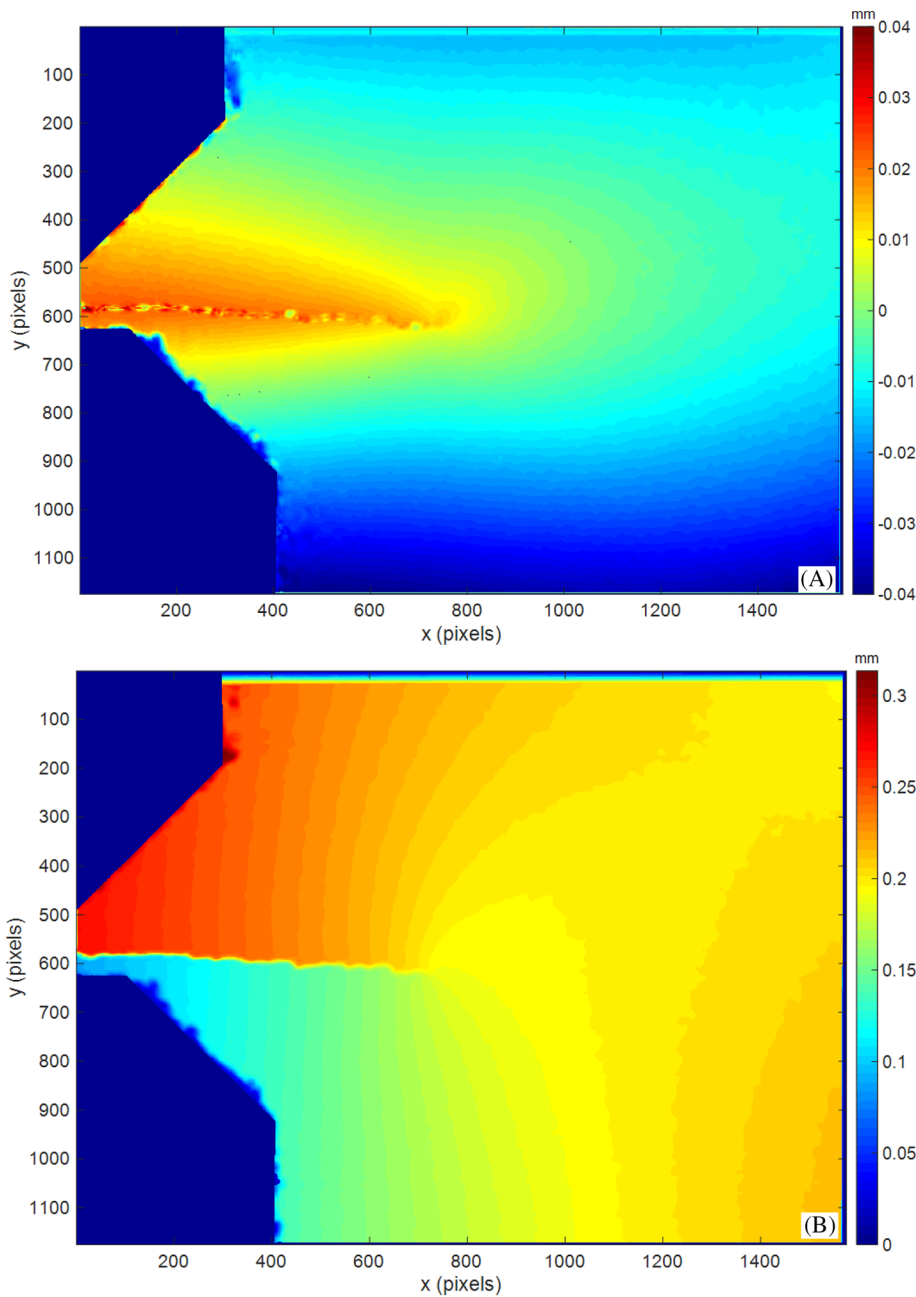


FIGURE 8 Example of displacement fields obtained by 2D digital image correlation (DIC) for a load of 600 N and a 9.13-mm crack: Horizontal (A) and vertical (B) displacement maps [Colour figure can be viewed at wileyonlinelibrary.com]

However, from Point C, the trend becomes nonlinear to Point D (maximum load, 600 N), which is linked to plastic deformation at the crack tip. The procedure followed to separate the CTOD into elastic and plastic components essentially requires extrapolating the linear regime between B and C to the point of maximum load (shown in Figure 10). The recommended practice in appendix X2 of the ASTM E 647 standard¹² formed the basis of the procedure used by the current authors in a previous work to obtain the elastic and plastic components of CTOD.³⁰ Considering the unloading half cycle, between D and E, the CTOD value linearly decreases with the same slope as that found between Points B and C for the loading half cycle. As the load is decreased below Point E, there is a

deviation from linearity due to the reversed plastic deformation.

The methodology described above to determine the elastic and plastic ranges of CTOD can be applied to analyze the CTOD data from all the tests. Figure 11 shows the results for the ranges of elastic and plastic CTOD obtained for the eight specimens tested as a function of the crack length. The elastic range data show significant scatter, whereas those corresponding to the plastic CTOD range show a less scattered and gradually increasing behavior as the crack propagates. This last behavior shows that the plastic CTOD range increases gradually with the crack length in the same way that the gradual development of plasticity in a growing fatigue crack at constant amplitude

FIGURE 9 Vertical displacement map with the region around the crack tip enlarged to show the location of the two points used to measure the crack tip opening displacement (CTOD). L_x is the horizontal distance behind the crack tip and L_y is the vertical distance from the crack plane [Colour figure can be viewed at wileyonlinelibrary.com]

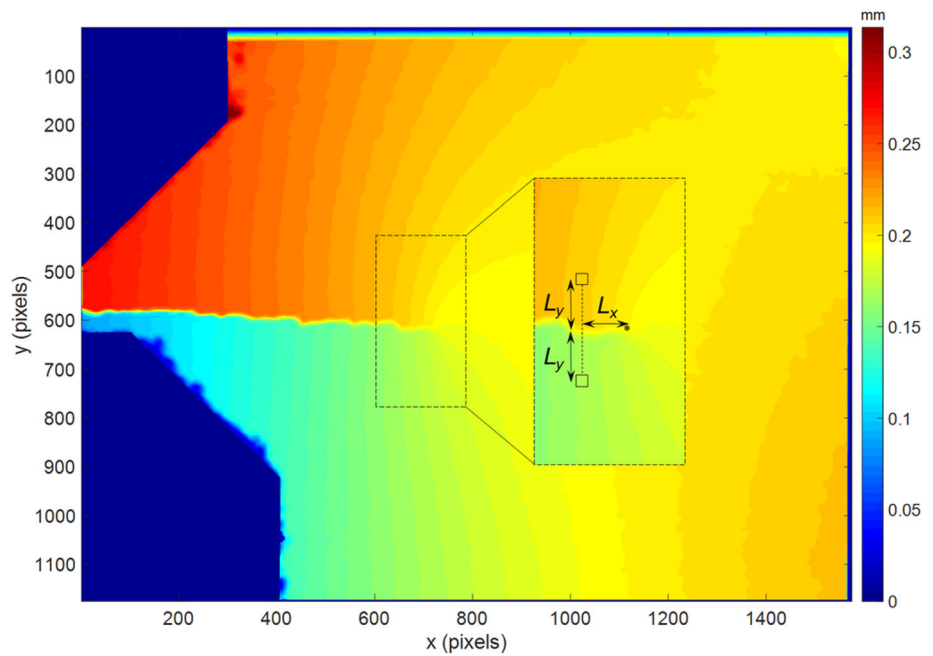
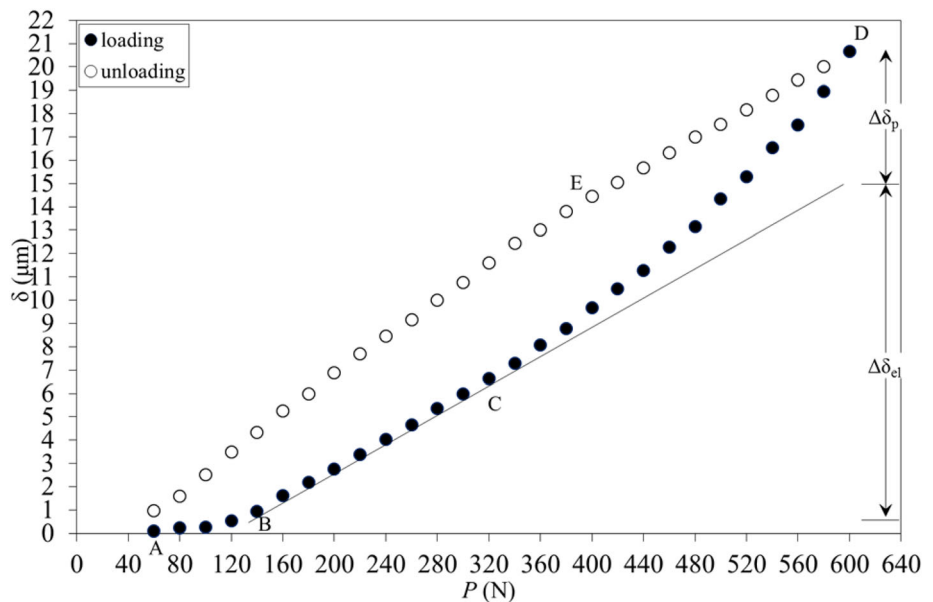


FIGURE 10 Variation in crack tip opening displacement (CTOD) throughout a full load cycle for the 7050-T6 aluminum specimen tested at $R = 0.1$ and for a crack length of 9.13 mm, showing the range of its elastic and plastic components [Colour figure can be viewed at wileyonlinelibrary.com]



loading cycle. Therefore, the plastic component of CTOD is linked to plastic deformation developed during fatigue crack propagation. In addition, higher values of plastic CTOD ranges are observed in the case of the specimens tested at low R ratio. Then, the lower the stress ratio, the higher the plastic CTOD range. This shows that there is an effect of the stress ratio on plastic deformation generated during fatigue crack growth, being greater in the tests performed at low stress ratio.

The influence of the measurement distance behind the crack tip (L_x) on the elastic and plastic ranges of CTOD ($\Delta\delta_e$, $\Delta\delta_p$) is shown in Figure 12. The elastic component shows a sudden increase with the L_x distance to

100 μm approximately, from which a stable value is reached. Zhu et al.³¹ also measured CTOD at different distances from crack tip in physically short cracks and obtained similar plots. A similar trend is observed for the plastic component, but less pronounced; there is an increase much smoother until reaching a stable value. This behavior can be linked with the plastic deformation generated in a growing fatigue crack. Plastic deformation smoothly increases from the crack tip until reaching its stabilization at a very short distance behind the crack tip. The ratio between the range of each component and the range of the total CTOD ($\Delta\delta_e/\Delta\delta_t$, $\Delta\delta_p/\Delta\delta_t$) is shown in Figure 12B. As indicated in the numerical study, the

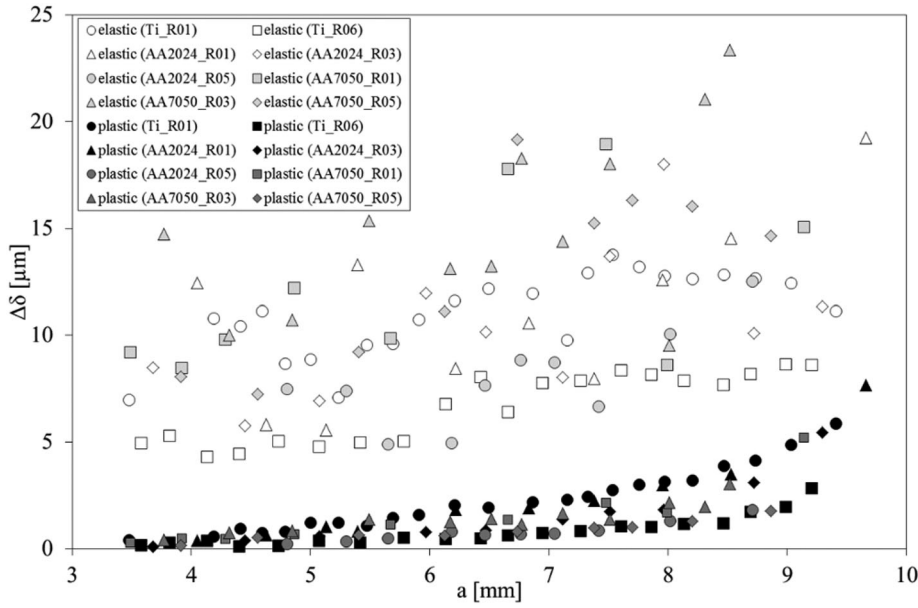


FIGURE 11 Ranges of elastic and plastic crack tip opening displacement (CTOD) along the crack length at different stress ratio values for the three materials tested in this work (CP titanium, AA2024-T3, and AA7050-T6)

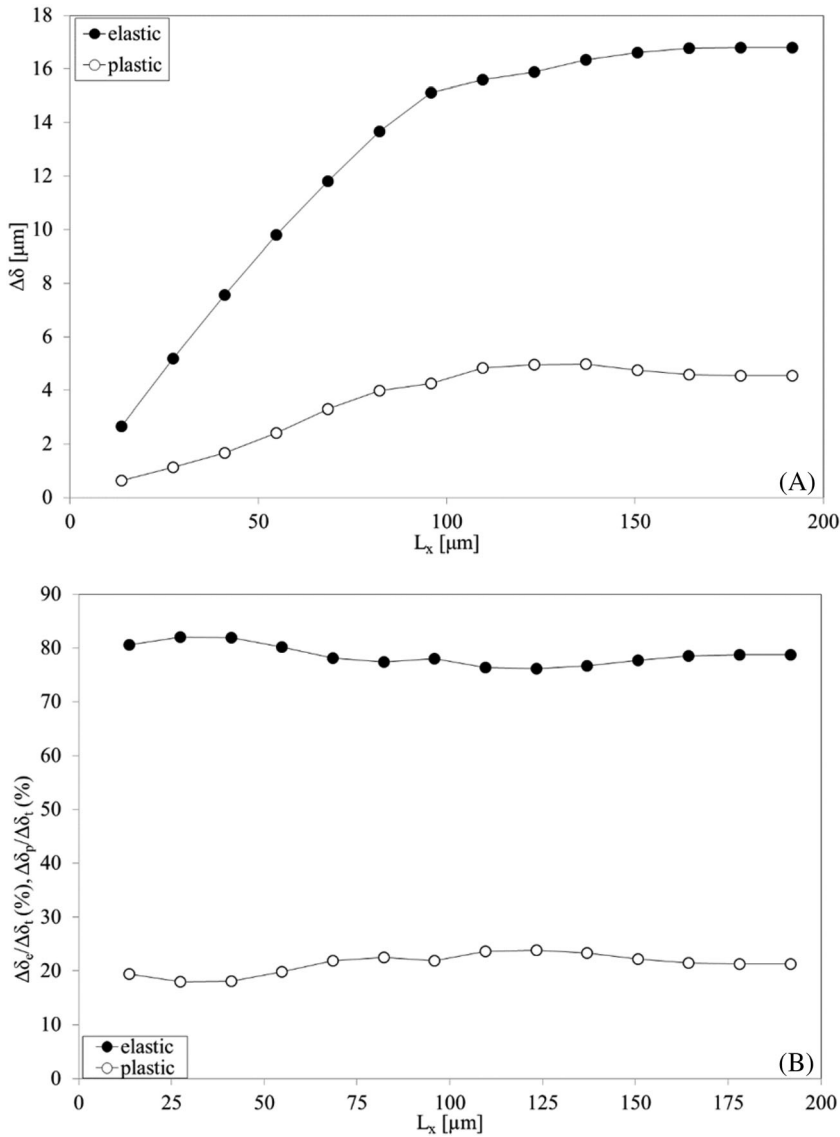
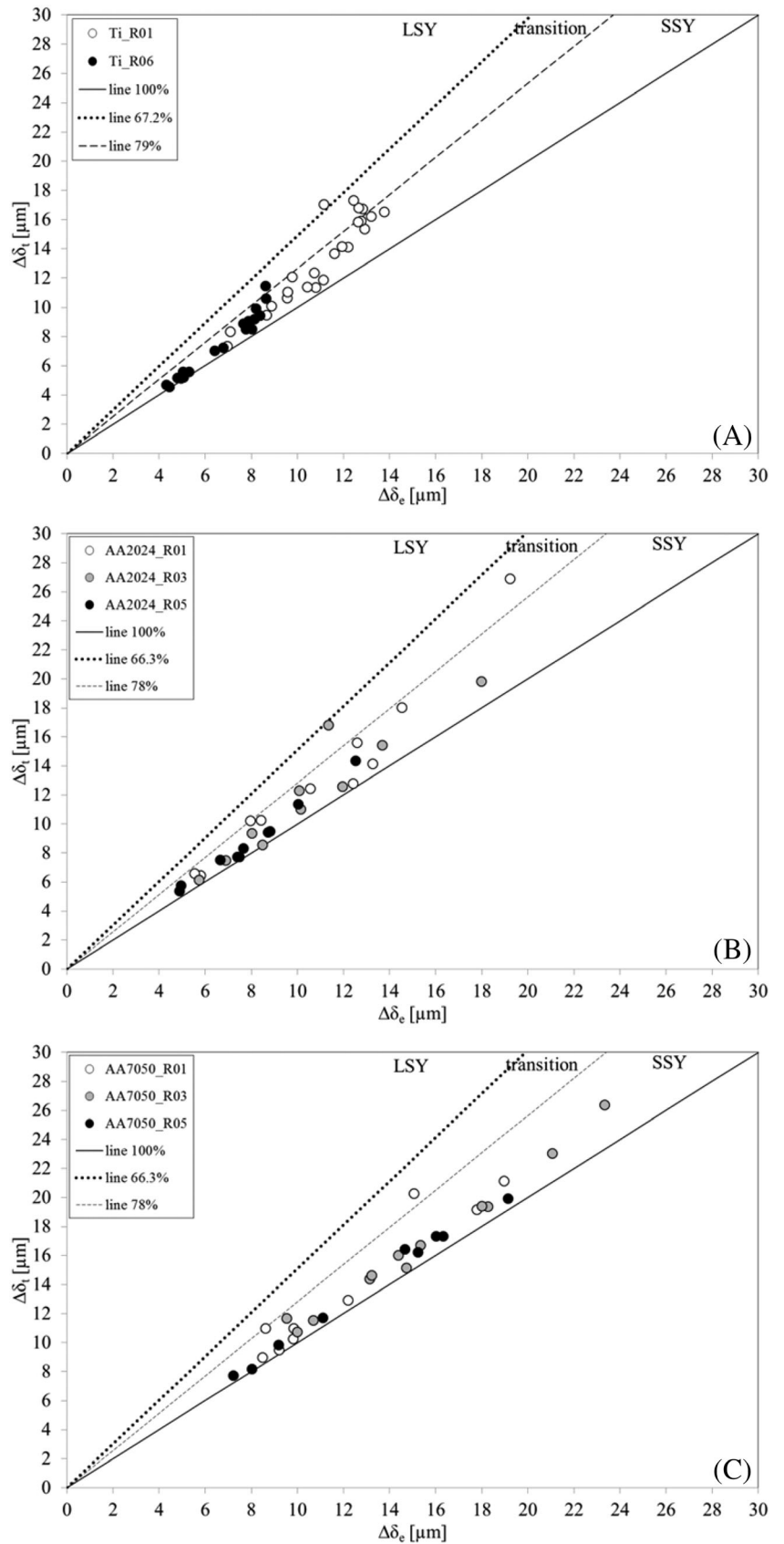


FIGURE 12 Influence of the distance behind the crack tip on the elastic and plastic ranges of crack tip opening displacement (CTOD). (A) $\Delta\delta_e$ and $\Delta\delta_p$ versus L_x and (B) $\Delta\delta_e/\Delta\delta_t$ and $\Delta\delta_p/\Delta\delta_t$ versus L_x . (Ti; $a = 9.40$ mm; $R = 0.1$)

FIGURE 13 Total crack tip opening displacement (CTOD) range as a function of its elastic range for titanium (A), 2024-T3 aluminum alloy (B) and 7050-T6 aluminum alloy (C). It is also plotted the boundary between small-scale yielding (SSY) and large-scale yielding (LSY) regimes for each material



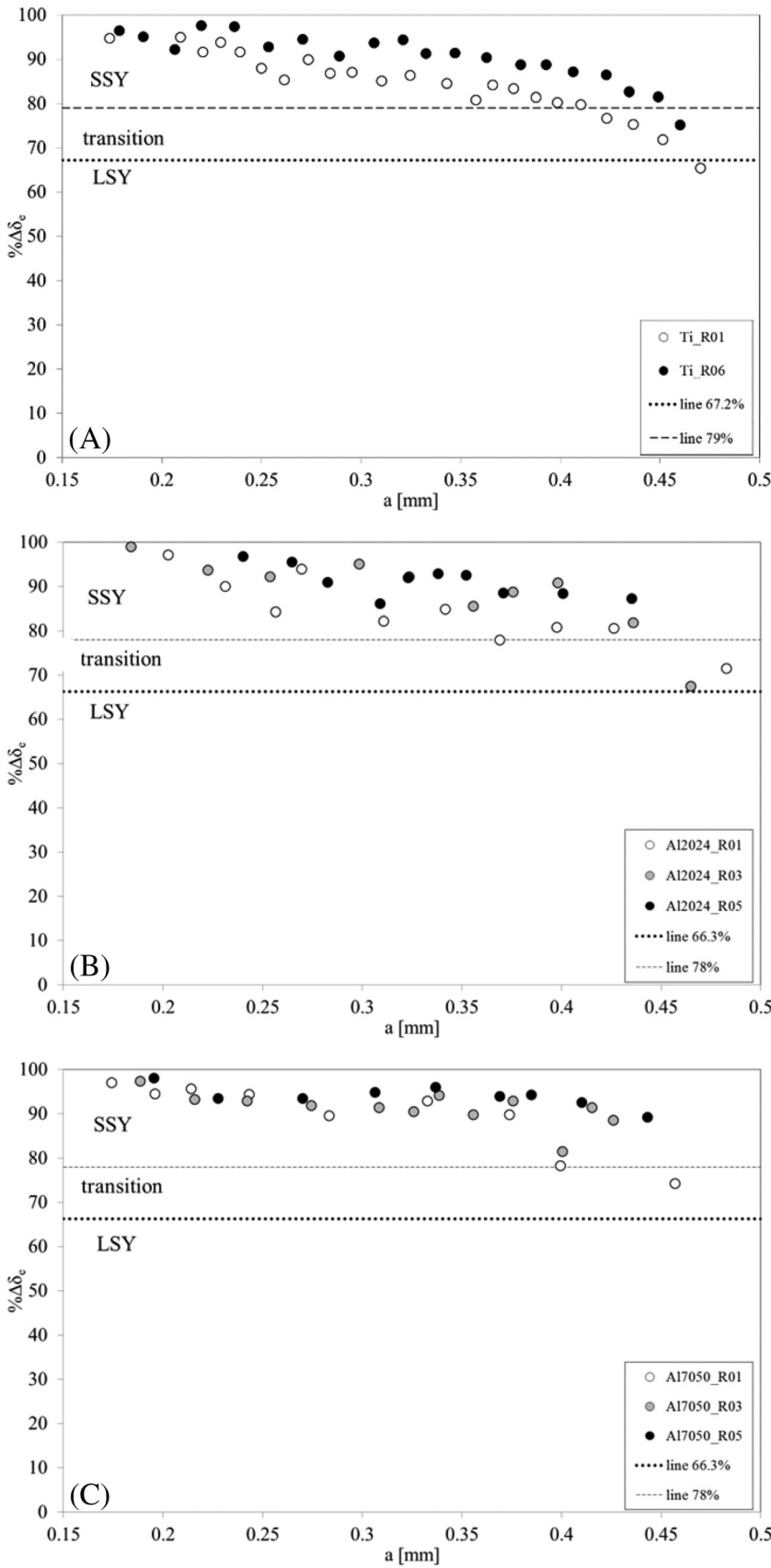


FIGURE 14 Ratio between the ranges of the elastic and total crack tip opening displacement (CTOD) ($\% \Delta \delta_e = \Delta \delta_e / \Delta \delta_t$) as a function of the crack length, normalized by the width of the specimen, for the three materials studied in this work: commercially pure titanium (A), 2024-T3 aluminum alloy (B) and 7050-T6 aluminum alloy (C). The boundaries to define the small-scale yielding (SSY) and large-scale yielding (LSY) regimes are also presented by a dashed and dotted lines, respectively

definition of the SSY boundary is performed from the analysis of the ratio between the elastic and total range of CTOD, which defines the parameter $\% \Delta \delta_e$.¹⁸ There is a stable behavior for both ratios ($\Delta \delta_e / \Delta \delta_t$, $\Delta \delta_p / \Delta \delta_t$), where the values are around a constant value. Therefore, it is clearly observed that there is no influence of the measurement points with the distance behind the crack tip (L_x) because the trend is practically constant. Thus, it is possible to obtain a mathematical fitting ($\% \Delta \delta_e = -0.0195L_x + 80.657$) to define the SSY boundary for the measurement distances used to estimate the CTOD for the titanium and aluminum alloys specimens. On the one hand, for L_x distances behind the crack tip of 68.5 and 123.2 μm , the SSY regime occurs if $\% \Delta \delta_e \geq 79\%$ and $\geq 78\%$, respectively. On the other hand, the LSY regime can be obtained from the interpolation of the boundaries predicted by Marques *et al.*,¹⁸ obtaining values of $\% \Delta \delta_e \leq 66.3\%$ and $\leq 67.2\%$ for L_x distances of 68.5 and 123.2 μm , respectively. In addition, the range between these percentages defines a transition regime from SSY to LSY.

Figure 13 shows the total CTOD range as a function of its elastic range for titanium (Figure 13A), 2024-T3 aluminum alloy (Figure 13B) and 7050-T6 aluminum alloy (Figure 13C). The region between 45° line and the dashed line corresponds to the region where SSY conditions are given; the region between the dashed line and the dotted line corresponds with the transition region between SSY and LSY conditions, while the region where LSY conditions can be considered correspond with the region on the left of the dotted line. For titanium, most of the cases are in SSY regime, a few cases are in the transition region and only one case is in LSY regime. Thus, three data points are in the transition region for the specimen tested

at $R = 0.1$ and only one data point in the case of the test at $R = 0.6$. In addition, the data point that is in LSY regime corresponds to the specimen tested at $R = 0.1$. This shows, therefore, that there is an effect of the stress ratio applied to conduct the test, being most likely to have SSY conditions for a high R -ratio value. This conclusion agrees with that above indicated where less plastic deformation is developed in high R tests, and therefore, it is easier for SSY conditions to be met. For the aluminum alloys, practically all the cases are in SSY regime, where just five cases are the transition region. There are not cases under LSY conditions. The effect of stress ratio is also observed in the aluminum specimens. The tests that present more cases out of the SSY region are those conducted at $R = 0.1$ and $R = 0.3$, whereas all cases for a stress ratio value of 0.5 are under SSY conditions.

All data points presented in Figure 13 correspond with all crack lengths studied. Therefore, in order to analyze the effect of crack length on establishing SSY conditions, Figure 14 shows the ratio between the elastic CTOD range and the total CTOD range ($\% \Delta \delta_e = \Delta \delta_e / \Delta \delta_t$) as a function of the crack length, normalized by the width of the specimen, marking by a dashed line the percentage defining the SSY conditions and by a dotted line the limit corresponding to the LSY regime. The conclusion established above of the stress ratio effect on SSY conditions it is also observed in the three graphs presented in Figure 14, where SSY conditions are more likely for low stress ratio values. There are more cases out the SSY region for long cracks, corresponding to crack lengths above a 40% respect to the specimen width. Therefore, it is evident the influence of crack length on the boundary between SSY and LSY, where an increase in crack length promote the onset of LSY. This behavior

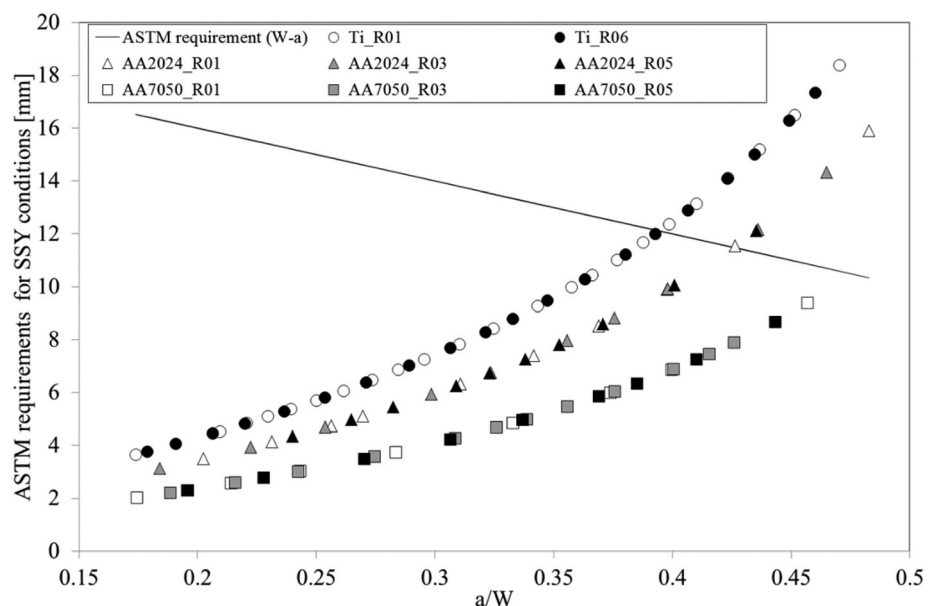


FIGURE 15 ASTM 647-15 requirements to promote small-scale yielding (SSY) conditions for the three materials studied. The $(4/\pi)(K_{max}/Y_0)^2$ specification for the three materials together with $W-a$ specification

agrees with the fact that as a fatigue crack is propagating, plastic deformation is increasing, and therefore, it moves towards LSY conditions.

The results can be compared with those obtained applying the requirements established for the CT specimen by ASTM E 647-15¹² according to Equation (1). Figure 15 graphically shows the requirements defined by ASTM E 647-15 for the three materials studied. $(4/\pi)(K_{max}/Y_0)^2$ specification for the three materials is presented together with W - a specification to carry out the comparison. Thus, the criterion is defined as those data points area above W - a line, do not meet SSY conditions. For the titanium specimens, the cases above $a/W = 0.4$ do not meet the SSY conditions; while for the AA2024-T3 specimens, the SSY conditions do not meet for a/W values above 0.43. In addition, according to ASTM standard, all data points meet the SSY conditions in the case of the AA7050-T6 specimens. According to this, there is a very good agreement between the experimental results and the requirements defined by ASTM. However, the ASTM requirements do not define a transition region between the SSY and LSY regimes as in the case of the criterion proposed in this work. In addition, it is observed again that long cracks promote LSY conditions.

5 | CONCLUSIONS

The use of K -based approaches to study FCG is valid only in the SSY regime. The boundary of SSY is normally checked comparing the size of plastic zone ahead of crack tip with the remaining ligament. An alternative approach uses the elastic and total CTOD, and a value $\Delta\delta_e/\Delta\delta_t = 75\%$ was proposed to be the lower boundary of SSY in a previous work,¹⁸ measured at a distance of 8 μm behind crack tip. DIC is very interesting and useful to study FCG and, in particular, the boundary of SSY regime. However, because the measurements of DIC are made at larger distances from crack tip, a study was developed to redefine the boundary of SSY based on CTOD, considering the position of measurement point relatively to crack tip. Three different materials have been studied (commercially pure titanium and 2024-T3 and 7050-T6 aluminum alloys), tested at different stress ratio values (0.1 and 0.6 for titanium, and 0.1, 0.3 and 0.5 for the aluminum alloys). The main conclusions driven are as follows:

- Numerically, the increase of L_x produces an increase of elastic deformation and a decrease of plastic CTOD range. This means that the separation of the measuring point relatively to the crack tip results in a loss of sensitivity to what goes on there. The variation is very

strong for low values of L_x , less than 50 μm , being smoother for longer distances. On the other hand, the distance perpendicular to crack tip has a limited effect on $\%\Delta\delta_e$.

- Experimentally, there is a very light influence on the ratio between the elastic and total ranges of CTOD ($\%\Delta\delta_e = \Delta\delta_e/\Delta\delta_t$) with the distance behind the crack tip to define the measurement points. The analysis of this trend allows to define the boundaries of SSY and LSY regimes. Thus, $\%\Delta\delta_e \geq 79\%$ and $\geq 78\%$ promote SSY conditions for titanium and 2024-T3 and 7050-T6 aluminum alloys, respectively. In addition, $\%\Delta\delta_e \leq 66.3\%$ and $\leq 67.2\%$ promote LSY conditions for titanium and 2024-T3 and 7050-T6 aluminum alloys, respectively.
- Of the cases analyzed, 90% are under SSY conditions. In addition, only one case of the 10% remaining is under LSY conditions, corresponding to the longest crack length ($a/W = 0.47$) analyzed for the titanium specimen tested at $R = 0.1$.
- Transition and/or LSY conditions are more probable in fatigue tests at low R -ratio values than in high R -ratio tests.
- Crack lengths above 40% respect to the width of the specimen promote transition or LSY conditions.

In the view of the authors, the results obtained in this investigation can assist to a better comprehension of the mechanisms driving fatigue crack growth.

ACKNOWLEDGMENTS

This research was funded by Portuguese Foundation for Science and Technology (FCT) under the project with reference PTDC/EME-EME/31657/2017 and by UIDB/00285/2020. The authors want to acknowledge the financial support from Junta de Andalucía through the research project “1380786” funded by the program “Proyectos de I+D+i en el Marco del Programa Operativo FEDER Andalucía 2014-2020. Convocatoria 2020”.

CONFLICT OF INTEREST

The authors declare that they have no known competing financial interests or personal relationships that could have appeared to influence the work reported in this paper.

AUTHOR CONTRIBUTIONS

Conception of the work: M. N. James, F. A. Díaz, F. V. Antunes; Data collection: E. R. A. Sérgio, J. M. Vasco-Olmo; Data analysis and interpretation: D. M. Neto, F. V. Antunes, J. M. Vasco-Olmo, F. A. Díaz; Drafting the article: J. M. Vasco-Olmo, F. V. Antunes; Critical revision of the article: F. A. Díaz, J. M. Vasco-Olmo.

DATA AVAILABILITY STATEMENT

The data that support the findings of this study are available on request from the corresponding author. The data are not publicly available due to privacy or ethical restrictions.

NOMENCLATURE

a	crack length
AA	aluminum alloy
CT	compact tension (specimen)
CTOD	crack tip opening displacement
DIC	digital image correlation
E	Young's modulus
FCG	fatigue crack growth
K	stress intensity factor
K_{max}	maximum stress intensity factor
K_{min}	minimum stress intensity factor
K_{open}	crack opening stress intensity factor
LEFM	linear elastic fracture mechanics
L_x	distance to crack tip measured along crack flank
L_y	distance to crack tip measured perpendicularly to crack flank
R	stress ratio
LSY	large-scale yielding
SSY	small-scale yielding
t	specimen's thickness
W	specimen's width
Y_0	initial yield stress
$\Delta\delta_e$	elastic CTOD range
$\Delta\delta_p$	plastic CTOD range
$\Delta\delta_t$	total CTOD range
ν	Poisson's ratio
ΔK	stress intensity factor range ($K_{max}-K_{min}$)
ΔK_{eff}	effective stress intensity factor range
$\%\Delta\delta_e$	ratio between $\Delta\delta_e$ and $\Delta\delta_t$, in percentage
$\%\Delta\delta_e$	value of $\%\Delta\delta_e$ at a distance of 8 μm behind crack tip
8 μm	

ORCID

Jose M. Vasco-Olmo  <https://orcid.org/0000-0002-2250-2306>

Francisco A. Díaz  <https://orcid.org/0000-0003-0467-542X>

REFERENCES

- Paris PC, Erdogan J. Critical analysis of crack growth propagation laws. *J Basic Eng.* 1963;85D(4):528-534. doi:10.1115/1.3656900
- Elber W. The significance of fatigue crack closure under cyclic tension. *ASTM STP.* 1971;486:230-242.
- Erdogan F, Ratwani M. Fatigue and fracture of cylindrical shells containing circumferential crack. *Int J Fract Mech.* 1970;4(4):379-392. doi:10.1007/BF00182626
- Nasgro, B. Fracture mechanics and fatigue crack growth analysis software. 2016.
- Clavel M, Pineau A. Fatigue behaviour of two nickel-base alloys I: experimental results on low cycle fatigue, fatigue crack propagation and substructures. *Mater Sci Eng.* 1982;55(2):157-171. doi:10.1016/0025-5416(82)90129-X
- Nicholls DJ. The relation between crack blunting and fatigue crack growth rates. *Fatigue Fract Eng Mater Struct.* 1994;17(4):459-467. doi:10.1111/j.1460-2695.1994.tb00245.x
- Schwalbe KH. Comparison of several fatigue crack propagation laws with experimental results. *Eng Fract Mech.* 1974;6(2):325-341. doi:10.1016/0013-7944(74)90031-9
- Vasudevan AK, Sadananda K, Louat N. Two critical stress intensities for threshold crack propagation. *Scr Metall Mater.* 1993;28(1):65-70. doi:10.1016/0956-716X(93)90538-4
- Kujawski D. A new $(\Delta K^+ K_{max})^{0.5}$ driving force parameter for crack growth in aluminum alloys. *Int J Fatigue.* 2001;23(8):733-740. doi:10.1016/S0142-1123(01)00023-8
- Noroozi AH, Glinka G, Lambert S. A two parameter driving force for fatigue crack growth analysis. *Int J Fatigue.* 2005;27(10-12):1277-1296. doi:10.1016/j.ijfatigue.2005.07.002
- Christopher CJ, James MN, Patterson EA, Tee KF. Towards a new model of crack tip stress fields. *Int J Fract.* 2007;148(4):361-371. doi:10.1007/s10704-008-9209-3
- American Society for Testing and Materials. *ASTM E 647-15. Standard Test Method for Measurement of Fatigue Crack Growth Rates.* American Society for Testing and Materials (ASTM); 2011.
- ISO. *ISO 12108. Metallic materials—fatigue testing – fatigue crack growth method.* International Organization for Standardization (ISO); 2012.
- Tada H, Paris PC, Irwin GR, American Society of Mechanical Engineers, ASM International. *The stress analysis of cracks handbook.* 3rd ed. ASME Press, Professional Engineering Pub., ASM International; 2000.
- Murakami Y. *Stress Intensity Factors Handbook.* Pergamon Press; 1987.
- Carpinteri A. *Handbook of Fatigue Crack Propagation in Metallic Structures.* Elsevier Science; 1994.
- Yasuoka T, Mizutani Y, Todoroki A. Small scale yielding conditions for steep residual stress distribution. *Eng Fract Mech.* 2012;96:392-400. doi:10.1016/j.engfracmech.2012.08.011
- Marques B, Borges MF, Antunes FV, Vasco-Olmo JM, Díaz FA, James MN. Boundaries of small-scale yielding regime. *Eng Fract Mech.* 2021;252:107806. doi:10.1016/j.engfracmech.2021.107806
- Marques B, Neto DM, Antunes FV, Vasco-Olmo JM, Díaz FA. Numerical tool for the analysis of CTOD curves obtained by DIC or FEM. *Fatigue Fract Eng Mater Struct.* 2020;43(12):2984-2997. doi:10.1111/ffe.13350
- Borges MF, Antunes FV, Neto DM, Vasco-Olmo JM, Díaz FA, James MN. Validity of small-scale yielding regime in notched geometries. *Int J Fatigue.* 2022;154:106563. doi:10.1016/j.ijfatigue.2021.106563
- Escalero M, Muniz-Calvente M, Zabala H, Urresti I. Suitability of constraint and closure models for predicting crack growth in generic configurations. *Eng Fract Mech.* 2020;225:106808. doi:10.1016/j.engfracmech.2019.106808

22. Frederick CO, Armstrong PJ. A mathematical representation of the multiaxial Bauschinger effect. *Mater High Temp.* 2007; 24(1):1-26. doi:10.3184/096034007X207589
23. Antunes FV, Serrano S, Branco R, Prates P. Fatigue crack growth in the 2050-T8 aluminium alloy. *Int J Fatigue.* 2018;115: 79-88. doi:10.1016/j.ijfatigue.2018.03.020
24. Antunes FV, Branco R, Prates PA, Borrego L. Fatigue crack growth modelling based on CTOD for the 7050-T6 alloy. *Fatigue Fract Eng Mater Struct.* 2017;40(8):1309-1320. doi: 10.1111/ffe.12582
25. Voce E. The relationship between stress and strain for homogeneous deformation. *J Inst Met.* 1948;74:537-562.
26. Borges MF, Antunes FV, Moreno B, Prates P, Camas D, Neto DM. Fatigue crack propagation analysis in 2024-T351 aluminium alloy using nonlinear parameters. *Int J Fatigue.* 2021; 153:106478. doi:10.1016/j.ijfatigue.2021.106478
27. Ferreira FF, Neto DM, Jesus JS, Prates PA, Antunes FV. Numerical prediction of the fatigue crack growth rate in SLM Ti-6Al-4V based on crack tip plastic strain. *Metals.* 2020;10(9): 1133. doi:10.3390/met10091133
28. Swift HW. Plastic instability under plane stress. *J Mech and Physics of Solids.* 1952;1(1):1-18. doi: 10.1016/0022-5096(52)90002-1
29. Borges MF, Neto DM, Antunes FV. Numerical simulation of fatigue crack growth based on accumulated plastic strain. *Theor Appl Fract Mech.* 2020;108:102676. doi:10.1016/j.tafmec.2020.102676
30. Vasco-Olmo JM, Díaz FA, Antunes FV, James MN. Characterisation of fatigue crack growth using digital image correlation measurements of plastic CTOD. *Theor Appl Fract Mech.* 2019; 101:332-341. doi:10.1016/j.tafmec.2019.03.009
31. Zhu M-L, Xuan F-Z, Tu S-T. Observation and modeling of physically short fatigue crack closure in terms of in-situ SEM fatigue test. *Mat Science & Eng.* 2014;A618:86-95. doi:10.1016/j.msea.2014.08.021

How to cite this article: Vasco-Olmo JM, Díaz FA, Neto DM, Sérgio ER, Antunes FV, James MN. Evaluation of small-scale yielding boundary using digital image correlation results. *Fatigue Fract Eng Mater Struct.* 2022;1-16. doi:10.1111/ffe.13674